Stem Cell Reports
Article

ISSCR

OPEN ACCESS

Impairment of Mitochondrial Calcium Buffering Links Mutations in *C9ORF72* and *TARDBP* in iPS-Derived Motor Neurons from Patients with ALS/FTD

Ruxandra Dafinca,[1,*] Paola Barbagallo,[1] Lucy Farrimond,[1] Ana Candalija,[1] Jakub Scaber,[1] Nida'a A. Ababneh,[1,2] Chaitra Sathyaprakash,[1] Jane Vowles,[3] Sally A. Cowley,[3] and Kevin Talbot[1,*]

[1]Nuffield Department of Clinical Neurosciences, University of Oxford, John Radcliffe Hospital, Oxford OX3 9DU, UK
[2]Cell Therapy Center, University of Jordan, Queen Rania St, 11942 Amman, Jordan
[3]James Martin Stem Cell Facility Sir William Dunn School of Pathology, University of Oxford, South Parks Road, Oxford OX1 3RE, UK
*Correspondence: ruxandra.dafinca@ndcn.ox.ac.uk (R.D.), kevin.talbot@ndcn.ox.ac.uk (K.T.)
https://doi.org/10.1016/j.stemcr.2020.03.023

SUMMARY

TDP-43 dysfunction is common to 97% of amyotrophic lateral sclerosis (ALS) cases, including those with mutations in *C9orf72*. To investigate how *C9ORF72* mutations drive cellular pathology in ALS and to identify convergent mechanisms between *C9ORF72* and *TARDBP* mutations, we analyzed motor neurons (MNs) derived from induced pluripotent stem cells (iPSCs) from patients with ALS. *C9ORF72* iPSC-MNs have higher Ca^{2+} release after depolarization, delayed recovery to baseline after glutamate stimulation, and lower levels of calbindin compared with CRISPR/Cas9 genome-edited controls. *TARDBP* iPS-derived MNs show high glutamate-induced Ca^{2+} release. We identify here, by RNA sequencing, that both *C9ORF72* and *TARDBP* iPSC-MNs have upregulation of Ca^{2+}-permeable AMPA and NMDA subunits and impairment of mitochondrial Ca^{2+} buffering due to an imbalance of MICU1 and MICU2 on the mitochondrial Ca^{2+} uniporter, indicating that impaired mitochondrial Ca^{2+} uptake contributes to glutamate excitotoxicity and is a shared feature of MNs with *C9ORF72* or *TARDBP* mutations.

INTRODUCTION

Amyotrophic lateral sclerosis (ALS) is a rapidly progressive and fatal neurodegenerative disorder. It is now clear that there is considerable genetic heterogeneity underlying ALS, with multiple genes independently acting as autosomal dominant risk alleles in approximately 10% of cases, while the majority of apparently sporadic cases do not have identified risk variants. However, despite etiological heterogeneity, 97% of cases are characterized by TDP-43 cytoplasmic aggregates at autopsy. A key unresolved question is, therefore, how different genetic factors converge on TDP-43 pathology. Because mutations in *TARDBP* can also lead to ALS with TDP-43 pathology, a comparison of genetic models based on these and other common mutations may reveal common pathways.

The commonest single genetic risk factor for ALS, and the related disorder frontotemporal dementia (FTD), is a $(GGGGCC)_n$ expansion in intron 1 of the *C9ORF72* gene, which accounts for 35%–40% of familial ALS cases, 5%–7% of sporadic ALS, and approximately 40% of familial FTD cases (DeJesus-Hernandez et al., 2011; Majounie et al., 2012; Renton et al., 2011). The number of $(GGGGCC)_n$ hexanucleotide repeats is typically >1,000 in affected individuals compared with <30 in healthy controls, although the threshold for triggering ALS has not been precisely established (van der Zee et al., 2013; Dedeene et al., 2019).

Motor neurons (MNs) derived from patient iPSCs have shown a range of phenotypes, including defects in autophagy, sequestration of RNA-binding proteins, endoplasmic reticulum (ER) stress, changes in gene transcription, and altered neuronal excitability, demonstrating that these models are potentially powerful tools to explore pathways relevant to the pathogenesis of ALS (Dafinca et al., 2016; Donnelly et al., 2013; Sareen et al., 2013).

Calcium signaling is an essential mechanism for normal neuronal function, transducing electrical activity into intracellular molecular signals, and there is evidence that low cytosolic Ca^{2+} buffering together with high Ca^{2+} influx during neurotransmission contribute to the vulnerability of MNs in ALS. Excessive Ca^{2+} influx during glutamatergic neurotransmission has previously been reported in both rodent models as well as iPS-derived neurons as a result of increased Ca^{2+} permeability of AMPA receptors (Couratier et al., 1993; Rothstein et al., 1990, 1992; Selvaraj et al., 2018). The regulation of elements involved in Ca^{2+} transients is therefore critical to the normal functioning of neurons, and one of the main factors buffering Ca^{2+} during signaling is the uptake by mitochondria of significant amounts of Ca^{2+} from the cytosol.

In this study, using iPS-derived MNs with the *C9ORF72* HRE, we have identified significant elevations in Ca^{2+} transients on depolarization and repeated firing in response to glutamate, and sustained high concentrations of cytosolic Ca^{2+}. We demonstrate this is due to increased calcium permeability of AMPA and NMDA receptors, deficiency in mitochondrial Ca^{2+} uptake, and reduced calcium buffering capacity, all of which are reversed by genome editing using CRISPR/Cas9-mediated homologous

recombination. We then compared these findings with iPS-derived MNs from ALS patients carrying the M337V mutation or I383T in the *TARDBP* gene, demonstrating that impairment of mitochondrial Ca^{2+} uptake is a common feature of ALS due to *C9ORF72* mutations and *TARDBP* mutations, while low ER Ca^{2+} levels correlate with low Ca^{2+} response in *TARDBP* MNs on depolarization.

RESULTS

Depolarization Induces High Intracellular Ca^{2+} in *C9ORF72* MNs and High Recovery Times, Rescued by Genome Editing

Fibroblasts from three healthy controls and three different ALS/FTD patients carrying mutations in *C9ORF72* were reprogrammed to induced pluripotent stem cells and differentiated to MNs using a previously published protocol, with modifications (Maury et al., 2015) (Figure S1). To analyze the response of *C9ORF72* MNs to depolarization and their Ca^{2+} buffering capacity, the neurons were exposed to 50 mM KCl for 30 s during live imaging of intracellular Ca^{2+} labeled by Fura 2-AM (Figures 1A and 1B). We measured the amplitude of Ca^{2+} peaks elicited and found that *C9ORF72* patient MNs released up to three times more Ca^{2+} into the cytosol compared with healthy MNs and 1.5 times more than the CRISPR/Cas9-corrected MNs (Figure 1C). Furthermore, we found that clearance of Ca^{2+} from the cytosol after depolarization was significantly delayed in *C9ORF72* MNs compared with healthy and CRISPR/Cas9-corrected lines (Figure 1D).

We then investigated the total level of Ca^{2+} ions in the stores of *C9ORF72* MNs using ionomycin, finding high levels of Ca^{2+} in both *C9ORF72* patient MNs and C9-Ed corrected MNs compared with the healthy controls, indicating that the intracellular levels of Ca^{2+} may account for the higher Ca^{2+} transients we detect upon depolarization (Figures 1E and 1F).

These results show that *C9ORF72* MNs release more Ca^{2+} into the cytosol after depolarization and have long delays in buffering cytosolic Ca^{2+}, but these phenotypes can be reversed by excision of the expanded repeat in the CRISPR/Cas9-edited MNs.

Glutamate Induces High-Frequency/Low-Amplitude Ca^{2+} Waves in *C9ORF72* MNs and Increases Their Susceptibility to Cell Death

Glutamate excitotoxicity, driven by a failure of reuptake of the neurotransmitter by adjacent astrocytes, is a potential mechanism of degeneration in ALS and may be implicated in neuronal death. To investigate the response of *C9ORF72* MNs to glutamate exposure, we examined the amplitude and recovery of Ca^{2+} waves after stimulation with 100 μM glutamate for 30 s (Figure 2A). MNs from *C9ORF72* patients generated significantly lower Ca^{2+} peaks compared with healthy and genome-edited controls (C9-Ed) (Figure 2B). Despite low release and intake of Ca^{2+}, the *C9ORF72* MNs required significantly longer time to recover to pre-stimulation cytosolic Ca^{2+} levels (Figure 2C).

Using 100 μM kainate, we stimulated the AMPA/kainate receptors, but did not observe consistent differences between *C9ORF72* patients and healthy controls (Figures S2A and S2B). To investigate the contribution of NMDA receptors to Ca^{2+} handling, the AMPA receptors were blocked by CNQX and we found that the amplitude of Ca^{2+} was higher in *C9ORF72* MNs (Figures 2D and 2E), and that their recovery time to baseline Ca^{2+} levels was up to three times longer, indicating that the NMDA receptors may contribute to increased Ca^{2+} permeability in *C9ORF72* MNs (Figure 2F).

One factor contributing to the delay in recovery is the increased excitability we detected in *C9ORF72* MNs. After stimulation with glutamate, the majority of healthy cells elicited two Ca^{2+} peaks, while *C9ORF72* MNs elicited up to seven peaks, with very few MNs showing only two peaks (Figure 2G). Prolonged exposure to lower levels of glutamate induced significantly increased cell death in *C9ORF72* MNs (Figure S2C).

Calcium binding proteins have a critical role in controlling cytosolic Ca^{2+} concentration by transporting Ca^{2+} ions across membranes, modulating Ca^{2+} levels, and acting as Ca^{2+} sensors. We analyzed calbindin, calreticulin, calpain-1, and calnexin expression and found a significantly reduced expression of calbindin in all *C9ORF72* MNs compared with controls (Figures 2G and S2D).

Therefore, despite a lower initial influx of Ca^{2+} in the cytosol in response to glutamate, *C9ORF72* MNs show a higher frequency of Ca^{2+} waves and a long delay in clearing released Ca^{2+} from the cytosol, partially due to low levels of cytosolic calcium buffering, which is likely to contribute to glutamate-induced cell death.

TARDBP MNs Show Hypoexcitability on Depolarization and Long Recovery Times after Glutamate Stimulation

To assess whether alterations in Ca^{2+} handling are specific to *C9ORF72* mutations, we studied the buffering capacity of *TARDBP* mutant iPS-derived MNs (Figure S3).

When depolarized by 50 mM KCl for 30 s, *TARDBP* MNs showed significantly lower Ca^{2+} amplitudes in response to depolarization and significantly increased recovery times (Figures 3A–3D). The amplitude of Ca^{2+} peaks was up to two times higher in *TARDBP* MNs after stimulation with glutamate (Figures 3E and 3F), and no differences were detected in the responses after CNQX

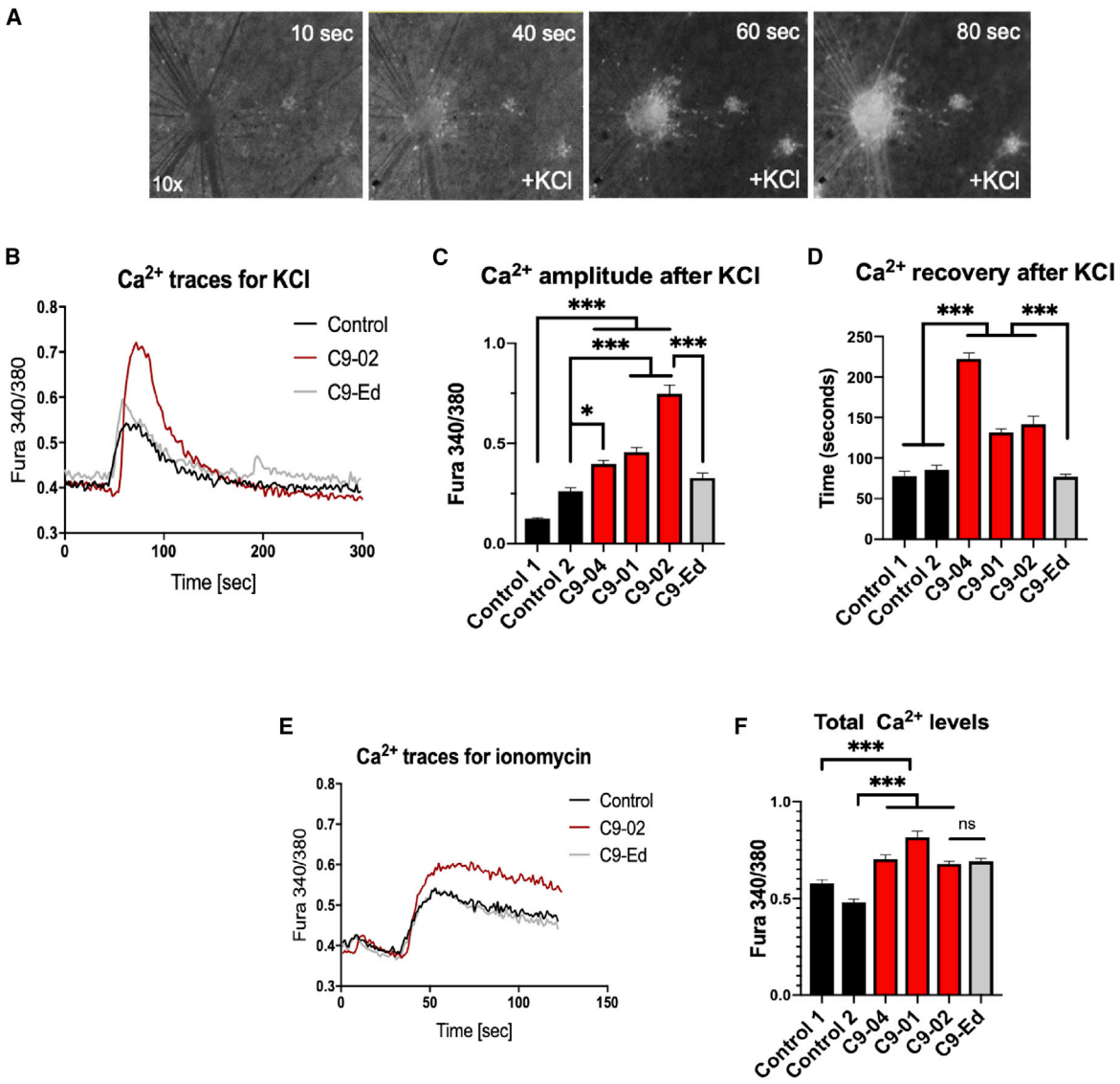

Figure 1. *C9ORF72* MNs Have High Ca^{2+} Transients and Recovery Times in Response to KCl

(A and B) Representative (A) images and (B) traces for Fura 340/380-loaded MNs after stimulation with 50 mM KCl.

(C) The amplitude of the first Ca^{2+} peak after stimulation with 50 mM KCl is higher in *C9ORF72* MNs compared with two healthy controls and two edited lines of MNs (C9-Ed) (*$p < 0.05$, ***$p < 0.001$); n = 25–73 neurons per iPS clone from at least two independent differentiations.

(D) Recovery of Ca^{2+} levels to baseline is delayed in *C9ORF72* MN (***$p < 0.001$); n = 25–127 neurons from two to four independent differentiations.

(E) Representative traces after ionomycin stimulation. (F) Total Ca^{2+} levels measured after stimulation with 5 μM ionomycin show significantly increased levels in all *C9ORF72* MNs as well as in the C9-Ed compared with healthy controls (***$p < 0.01$); n = 25–78 neurons from two to three independent differentiations. Data are shown as mean ± SEM with one-way ANOVA and Dunnet's *post hoc* tests.

See also Figure S1.

block of the Ca^{2+}-permeable AMPA receptors between controls and TDP-43^{M337V} MNs. However, blocking the NMDA receptors with 10 μM memantine resulted in significantly higher Ca^{2+} levels in TDP^{M337V} compared with healthy controls, while no differences were observed between C9orf72 and healthy controls or C9-Ed (Figure S4A). Similar to *C9ORF72* MNs, we recorded a significant delay in the recovery to baseline Ca^{2+} levels after glutamate exposure, up to two times longer than healthy controls (Figure 3G). The frequency of Ca^{2+} peaks was also higher in TDP-43^{M337V} MNs compared with controls (Figure 3H), but we did not detect

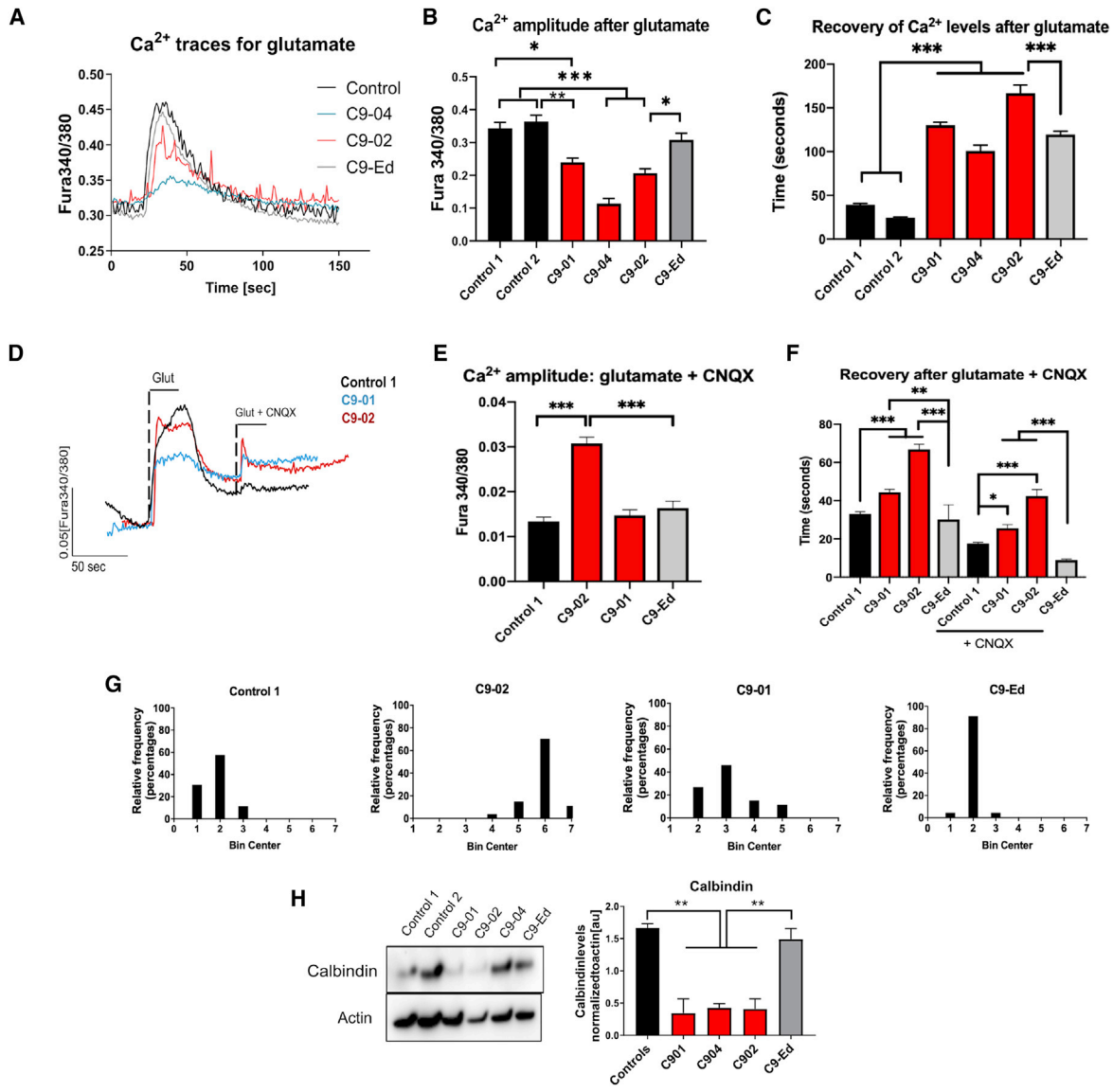

Figure 2. Glutamate Induces Frequent, Low Ca^{2+} Waves in *C9ORF72* MNs and Ca^{2+} Levels Remain Increased in the Cytosol Contributing to Glutamate-Induced Cell Death

(A) Representative Fura 340/380 traces in response to glutamate stimulation.

(B) Amplitude of Ca^{2+} peaks in *C9ORF72* MNs is lower than healthy controls and C9-Ed MNs (**p < 0.01, ***p < 0.001); n = 23–78 neurons from two independent differentiations.

(C) Recovery of Ca^{2+} levels to baseline is significantly increased in *C9ORF72* MNs compared with healthy controls and is improved in C9-Ed MNs (***p < 0.001); n = 26–151 neurons from two to four independent differentiations.

(D) Representative Fura 340/380 traces in response to glutamate stimulation followed by CNQX and glutamate.

(E and F) (E) Ca^{2+} amplitude and (F) Ca^{2+} recovery times are significantly higher in C9orf72 MNs after blocking the AMPA receptors with CNQX (*p < 0.05, **p < 0.01, ***p < 0.001); n = 11–24 neurons from two independent differentiations.

(G) Distribution of Ca^{2+} peaks elicited by glutamate stimulation in healthy controls, *C9ORF72* MNs, and C9-Ed.

(H) Immunoblotting shows low levels of calbindin in *C9ORF72* MNs compared with healthy and genome-edited C9-Ed (**p < 0.01). Data are shown as mean ± SEM with one-way ANOVA and Sidak's *post hoc* tests.

differences in the expression of any calcium buffering proteins in TDP-43^{M337V} or TDP-43^{I383T} MNs (Figures S4B and S4C).

These results confirm that, convergent with *C9ORF72* mutations, *TARDBP* MNs demonstrate significant delays in buffering cytosolic Ca^{2+} and glutamate hyperexcitability.

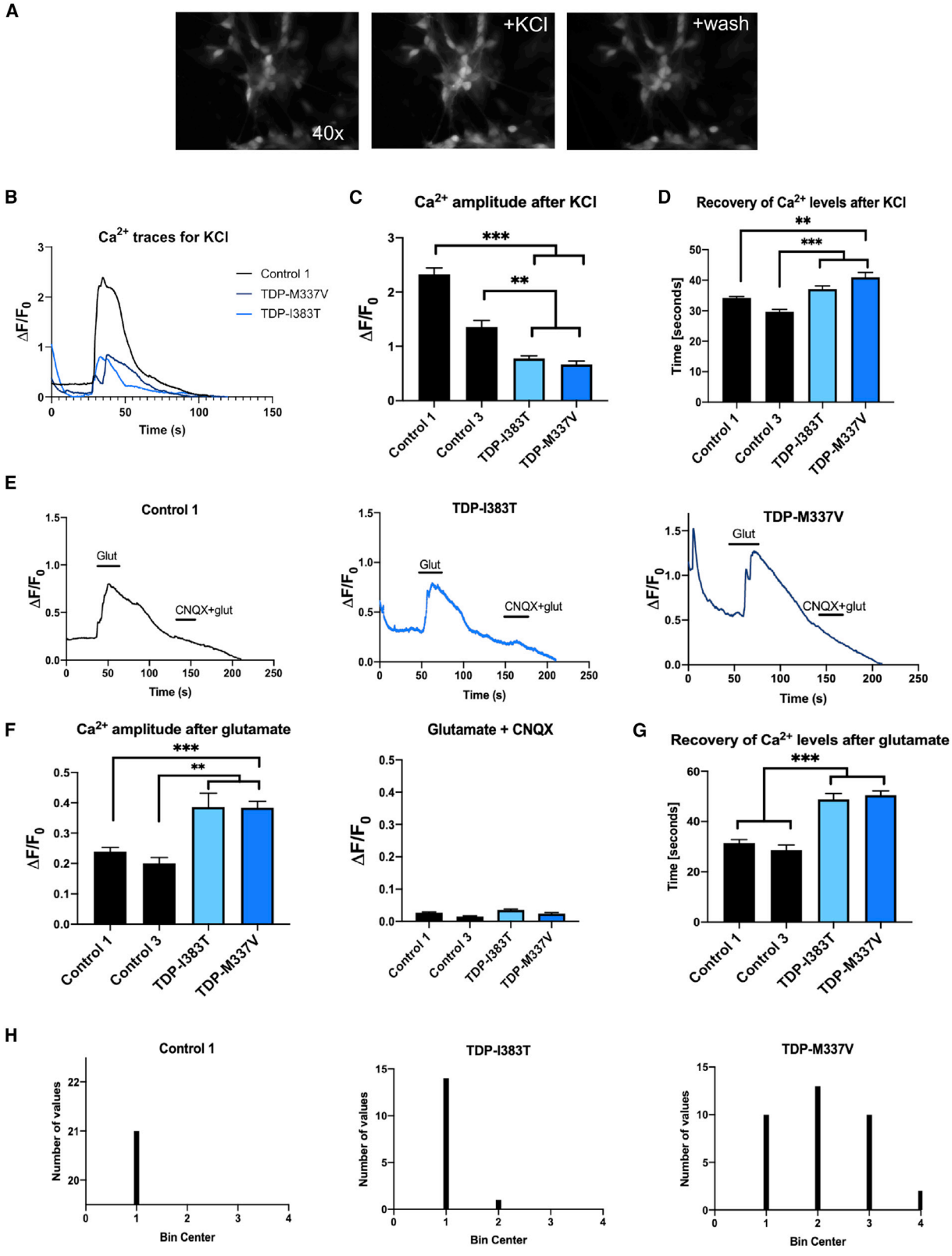

(legend on next page)

We also detect alterations in Ca^{2+} responses after depolarization, which show low levels in *TARDBP* and high levels in *C9ORF72* MNs compared with healthy controls.

Ca^{2+}-Permeable AMPA-R and NMDA-R Subunits Are Upregulated in *C9ORF72* and TDP-43^{M337V} iPS-Derived MNs

Previous studies have shown that glutamate receptors are expressed at a higher level in *C9ORF72* iPS MNs, along with age-dependent glutamate sensitivity and hyperexcitability (Bursch et al., 2019; Devlin et al., 2015; Donnelly et al., 2013; Sareen et al., 2013; Selvaraj et al., 2018). To analyze whether the expression of these receptors is altered and could account for increased vulnerability of *C9ORF72* and TDP-43^{M337V} MNs to glutamate excitotoxicity, we used RNA sequencing data generated from 28-day-old C9-02 iPSC-derived MN cultures as well as from the edited clones derived from the same cell line (C9-Ed) and 30-day-old TDP-43^{M337V} MNs (three clones, 03-03, 03-04, and 03-06). RNA sequencing was performed in TDP-43^{M337V} and key results were validated in TDP-43^{I383T} MNs.

Differential expression analysis demonstrated a significant increase in the expression of AMPA receptor *GRIA3* mRNA in *C9ORF72* mutant iPSC-derived MNs, validated by qPCR (Figure 4A). Subunits 1 and 3 are known to increase the calcium permeability of this receptor and are balanced by the expression of AMPA receptor subunit 2, which has been shown to decrease calcium permeability. AMPA subunit 2 (*GRIA2*) was also found to be upregulated in *C9ORF72* MNs compared with C9-Ed, suggesting a compensatory mechanism to balance the increase in Ca^{2+} permeability from *GRIA1* and *GRIA3*. In TDP-43^{M337V} MNs analyzed at a similar time point, we detected significantly increased expression of AMPA receptor *GRIA4*, which is a Ca^{2+}-permeable ligand-gated ion channel mediating excitatory synaptic transmission in the presence of L-glutamate (Figures 4B and S4B).

In *C9ORF72* MNs, significantly increased expression was seen in NMDA-R subunit 2A (*GRIN2A*), and a similar non-significant trend was observed in subunits 1 and 2B (*GRIN1, GRIN2B*) (Figure 4C). *GRIN1* and *GRIN2B* were also significantly increased in TDP-43^{M337V} MNs and validated by qPCR (Figures 4D and S4B).

In addition to fast ionotropic receptors, glutamate also acts on metabotropic receptors (mGluR or GRM), which generate slower postsynaptic responses. *GRM4* transcript expression was significantly increased in *C9ORF72* iPSC-derived MNs compared with edited controls (Figure 4E). We also showed by qPCR a similar elevation in *GRM2*, both of which are believed to attenuate glutamate toxicity via a decrease in cAMP levels (Figure 4E). In TDP-43^{M337V}, we detected an upregulation of *GRM3*, which is also implicated in the inhibition of cAMP (Figure 4F).

These results show a consistent upregulation of Ca^{2+}-permeable subunits of glutamate receptors in both *C9ORF72* and *TARDBP* MNs, but suggest that the two mutations have different regulatory mechanisms for Ca^{2+} sensitivity.

Mitochondria Do Not Efficiently Clear Ca^{2+} from the Cytosol in *C9ORF72* MNs due to Low Levels of MCU and MICU2

Increased cytosolic Ca^{2+} initiates a series of events, which include mitochondrial Ca^{2+} overload (Peng et al., 1998), generation of reactive oxygen species, and release of cytochrome *c*. To analyze whether deficiencies in Ca^{2+} uptake into mitochondria account for the observed delays in clearing cytosolic Ca^{2+}, we investigated the dynamics of mitochondrial Ca^{2+} after stimulation with glutamate and caffeine of neurons loaded with Rhod 2-AM (Figure 5A). *C9ORF72* mutant MNs exposed to 100 μM glutamate

Figure 3. *TARDBP* MNs Show Low Levels of Cytosolic Ca^{2+} on Depolarization and High Cytosolic Ca^{2+} after Glutamate Stimulation

(A and B) (A) Fluo-4 AM-loaded MNs responding to KCl and (B) representative Ca^{2+} traces.

(C) Depolarization with 50 mM KCl induces low Ca^{2+} waves in *TARDBP* iPS-derived MNs compared with healthy controls (**$p < 0.01$, ***$p < 0.001$) n = 33–112 neurons from two to four independent differentiations.

(D) Recovery to baseline Ca^{2+} levels is slower in *TARDBP* MNs compared with healthy controls (***$p < 0.001$); n = 33–51 neurons from two to four independent differentiations.

(E) Ca^{2+} traces after stimulation with 100 μM glutamate and CNQX.

(F) Higher amplitude Ca^{2+} waves are detected in TDP-43^{M337V} compared with the healthy controls (****$p < 0.001$); n = 30–142 neurons from two to four independent differentiations. No differences are detected after CNQX; n = 30–83 neurons from two independent differentiations.

(G) Recovery of baseline Ca^{2+} levels after stimulation with glutamate is higher in *TARDBP* MNs (***$p < 0.001$); n = 52–128 neurons from two to four independent differentiations.

(H) Distribution of the number of peaks elicited in response to glutamate stimulation. Data are presented as mean ± SEM with one-way ANOVA and Sidak's *post hoc* tests.

See also Figure S3.

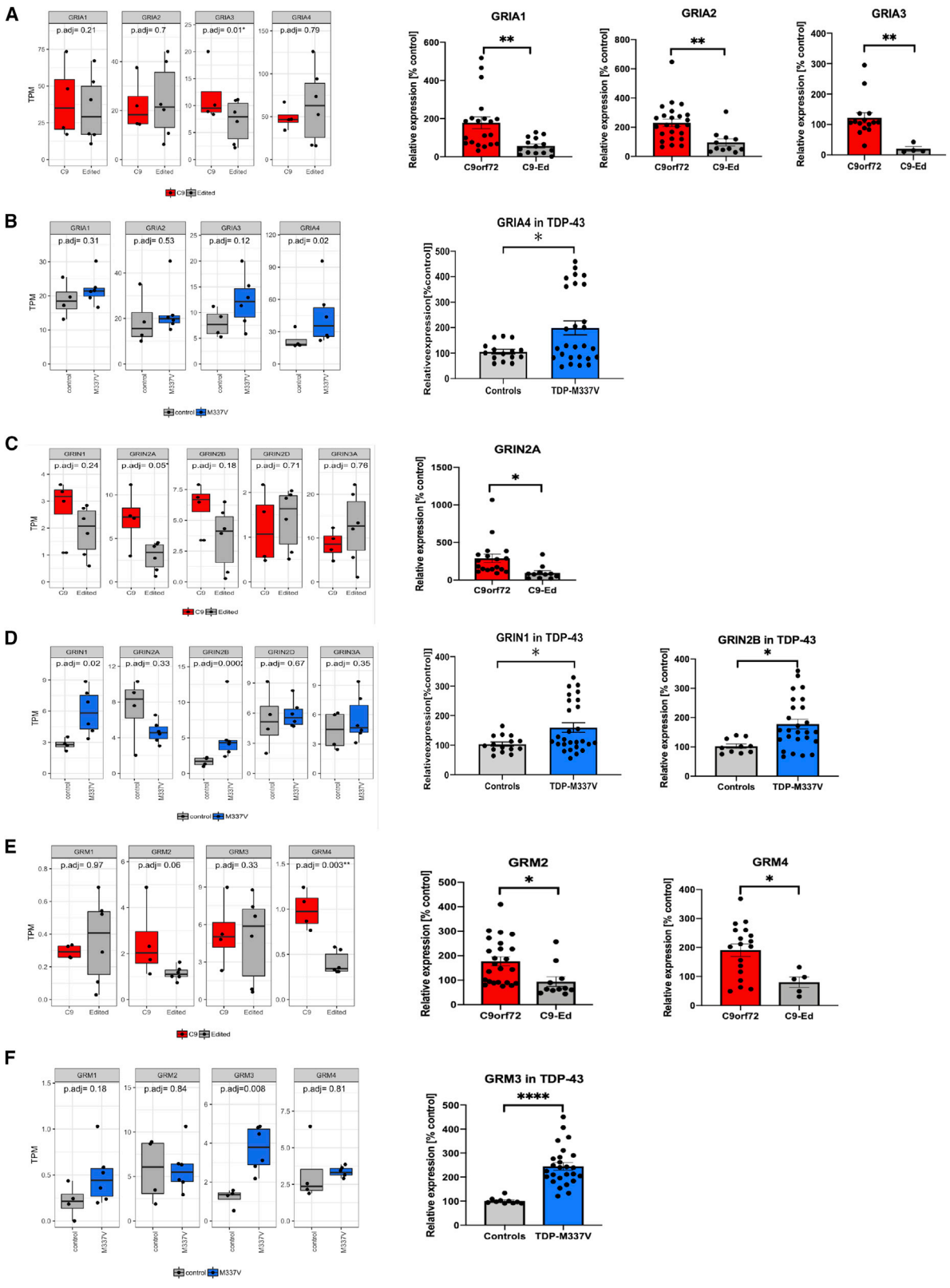

(legend on next page)

showed significantly reduced uptake of Ca^{2+} into mitochondria compared with healthy and C9-Ed MNs (Figures 5B and 5C). When stimulated with 20 mM caffeine, which opens ryanodine receptors on the ER, the uptake of Ca^{2+} into the mitochondria of *C9ORF72* mutant MNs was reduced by half compared with healthy MNs and C9-Ed MNs (Figure 5D).

To confirm these findings, we analyzed total cytosolic Ca^{2+} during stimulation with glutamate followed by immediate addition of carbonyl cyanide m-chlorophenyl hydrazine (CCCP) to release mitochondrial Ca^{2+} (Figures 5E and 5F). The addition of the protonophore CCCP immediately after cell stimulation has been shown in many cell types to produce a large increase in cytosolic Ca^{2+} due to release of the Ca^{2+} accumulated by mitochondria (Herrington et al., 1996; Werth and Thayer, 1994). Using this method, we recorded significantly smaller Ca^{2+} peaks in the *C9ORF72* patient MNs after CCCP stimulation compared with healthy control MNs, which released at least double the amount of mitochondrial Ca^{2+} (Figures 5E and 5F).

Mitochondria take up Ca^{2+} from the cytosol via the Ca^{2+} uniporter (MCU), which is a specific calcium pathway driven by the difference in electrical potential across the mitochondrial membrane. We found a significant decrease in its protein expression in *C9ORF72* MNs (Figures 5G and 5H), which is not due to fewer mitochondria present in the *C9ORF72* MNs verified using TOMM20 immunoblotting (Figure S5). Using RNA sequencing, we detected that one of the two gatekeeping proteins regulating MCU activity, MICU2, was significantly downregulated in C9-02 and rescued by the correction of the mutation in C9-Ed (Figure 5I), which we confirmed by immunoblotting and qPCR (Figures 5J and 5K).

These results suggest that the reduced uptake of Ca^{2+} from the cytosol after stimulation in *C9ORF72* MNs is partly due to deficiency in mitochondrial Ca^{2+} buffering as a result of low expression of the mitochondrial Ca^{2+} uniporter and its regulatory MICU2.

TARDBP MNs Have Reduced Mitochondrial Ca^{2+} Uptake Capacity

Mitochondrial Ca^{2+} uptake was similarly assessed in *TARDBP* MNs. After stimulation with CCCP, we detected significantly lower levels of Ca^{2+} released from mitochondria in mutant lines compared with healthy controls (Figures 6A and 6B). RNA sequencing in TDP-43^{M337V} MNs showed a significant upregulation of the mitochondrial Ca^{2+} uptake regulator *MICU1*, which we confirmed by qPCR, with no differences in the expression of *MICU2* (Figure 6C). The I383T mutation was not included in RNA sequencing and MICU1 levels were analyzed by western blotting (Figure S6A). In contrast to the *C9ORF72* MNs, normal levels of MCU were detected in all *TARDBP* iPS-derived MNs (Figure 6D).

To investigate the deficits in mitochondrial function in comparison with the *C9ORF72* MNs, we analyzed mitochondrial membrane potential using MitoTracker (Figure 6E). Our previous work had shown that *C9ORF72* iPS-derived MNs have significant morphological alterations and reduced potential of the mitochondria, but in TDP-43^{M337V} MNs assessment of mitochondrial membrane potential revealed no differences between the healthy controls and patient MNs (Figure 6F).

These results show that impaired mitochondrial Ca^{2+} buffering is a common pathomechanism between *C9ORF72* and *TARDBP* mutations and that an imbalance between the regulatory proteins MICU1 and MICU2

Figure 4. Ca^{2+} Permeable Subunits of the Glutamatergic Receptors AMPA and NMDA Are Overexpressed in *C9ORF72* MNs and TDP-43^{M337V} MNs

(A) RNA sequencing (RNA-seq) results in *C9ORF72* and C9-Ed iPS-derived MNs for AMPA receptor subunits 1–4 (*GRIA1–4*) and qPCR validation of higher expression of *GRIA1*, *GRIA2*, and *GRIA3* in *C9ORF72* MNs (two or three patients pooled together) compared with C9-Ed (one or two clones) (**p < 0.01, Student's t test).

(B) RNA-seq of AMPA receptor subunits 1–4 (*GRIA1–4*) in TDP-43^{M337V} and qPCR validation of *GRIA4* showing increased expression in patients versus healthy controls (*p < 0.05, Student's t test).

(C) RNA-seq results for NMDA receptor subunits 1–3A (*GRIN1–3*) and qPRC validation of *GRIN2A* elevation in *C9ORF72* MNs (three patients) compared with C9-Ed (*p < 0.05, Student's t test).

(D) RNA-seq results for NMDA receptor subunits 1–3A in TDP-43^{M337V} MNs compared with healthy controls and qPCR validating high levels of *GRIN1* and *GRIN2B* in TDP-43^{M337V} (*p < 0.05, Student's t test).

(E) RNA-seq results for metabotropic glutamate receptors 1–4 (*GRM1–4*) and qPCR validating increased expression of *GRM2* and *GRM4* in *C9ORF72* MNs (two or three patients) compared with C9-Ed (*p < 0.05, Student's t test).

(F) RNA-seq results for *GRM1–4* in TDP-43^{M337V} and qPCR validating increased expression of *GRM3* in TDP-43^{M337V} compared with healthy controls (****p < 0.001, Student's t test). Normalized transcript per million (TPM) values are reported on the y axis and allow estimation of relative abundances of the transcription of each gene. Adjusted p values (p. adj) are derived from the differential expression analysis performed using *DESeq2* and represent Benjamini-Hochberg corrected p values. Asterisks indicate p values below 0.05. qPCR data are presented as mean ± SEM. N = 3 independent differentiations for all iPS lines shown.

See also Figure S3.

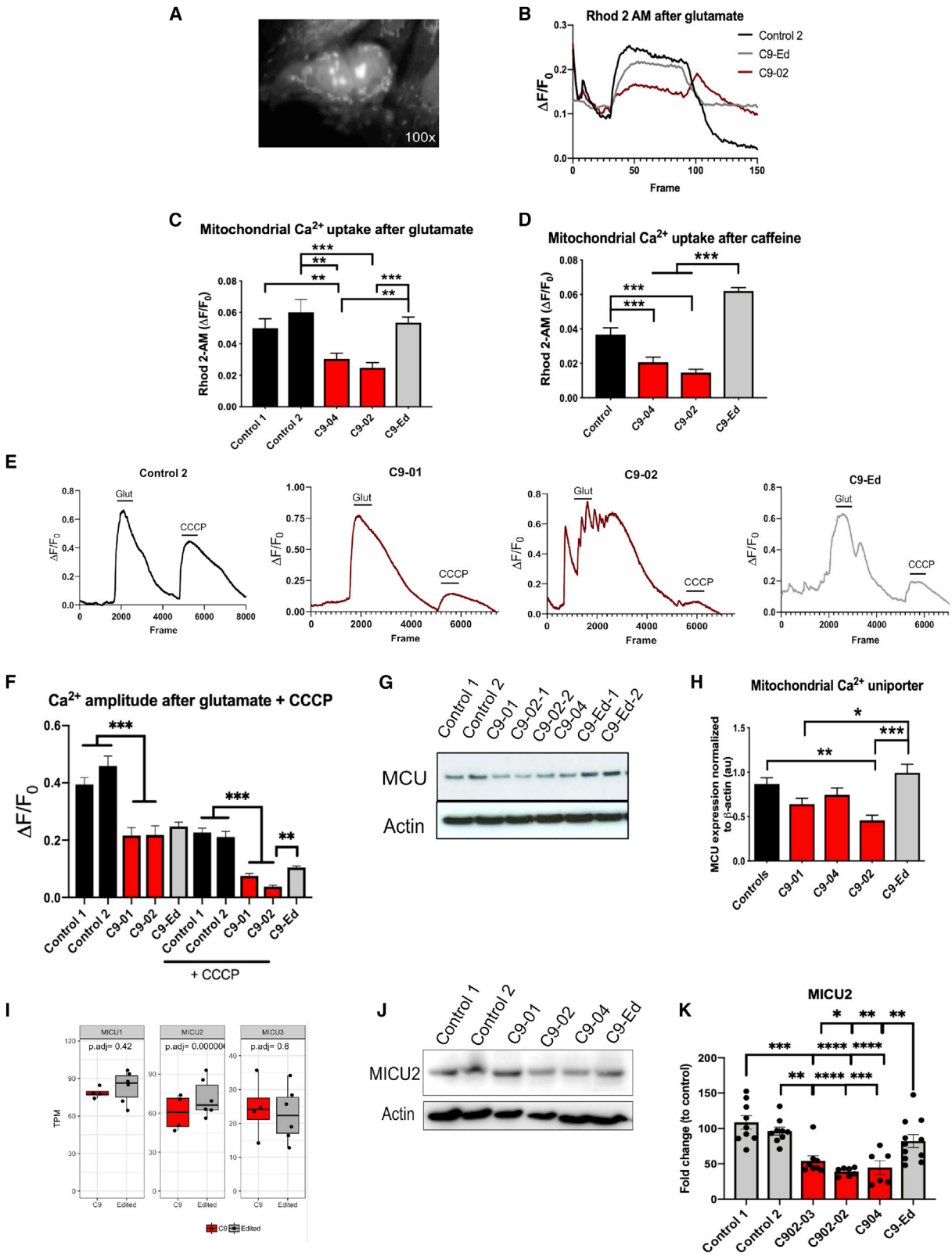

(legend on next page)

plays an important role in the reduction of mitochondrial Ca^{2+} uptake.

C9ORF72 and *TARDBP* MNs Have Low ER Ca^{2+} Release

The regulation of Ca^{2+} signaling is one of the most important functions of ER-mitochondria crosstalk (Filadi et al., 2017). We previously reported high levels of Ca^{2+} in the ER of *C9ORF72* iPS-derived MNs (Dafinca et al., 2016). To investigate ER Ca^{2+} homeostasis in *TARDBP* MNs and *C9ORF72* MNs, the neurons were perfused with carbamylcholine to activate the acetylcholine receptors and stimulate ER Ca^{2+} release through IP_3R (Figure 7A). Both *TARDBP* MNs and *C9ORF72* MNs responded with significantly lower release of ER Ca^{2+} compared with healthy controls (Figure 7A). The levels of IP_3Rs were not different between the genotypes, suggesting that the differences in Ca^{2+} release in *TARDBP* MNs are mainly due to low levels of ER Ca^{2+} stores that we detected after stimulation with 10 μM thapsigargin (Figures 7B, S6B, and S6C). We also investigated whether altered regulation of ER Ca^{2+} induces ER stress, but we did not detect increases in GRP78/BiP in TDP-43^{M337V} MNs (Figure S6D). Furthermore, we analyzed the localization of TDP-43 to investigate a potential mechanism where cytoplasmic mislocalization contributes to the similar phenotypes observed in *C9ORF72* and *TARDBP* MNs, but we did not detect mislocalization in any of the patient lines at baseline (Figure S7).

ER Ca^{2+} release is under the regulation of the antiapoptotic Bcl-2 family of proteins and we have previously shown that its levels were significantly increased in a cell model (HEK293) that expressed the entire genomic locus of *TARDBP* with M337V (Mutihac et al., 2015). Consistent with our previous findings, human iPS-derived MNs from the TDP-43^{M337V} patient showed significantly increased levels of Bcl-2 expression (Figure 7C), confirming that ER Ca^{2+} homeostasis is disrupted in TDP-43^{M337V} MNs and that low ER Ca^{2+} may contribute to low Ca^{2+} release on depolarization in TDP-43^{M337V} MNs.

DISCUSSION

In a previous phenotypic characterization of *C9ORF72* iPS-derived MNs, we described increased expression of markers of stress granule formation, activation of cellular death pathways (cleaved caspase-3, cytochrome *c*), and mitochondrial dysregulation (Dafinca et al., 2016). In this study, we focused on the physiological implications of the *C9ORF72* mutation in iPS-derived MNs from patients compared with isogenic control lines generated by CRISPR/Cas9 where the pathogenic hexanucleotide expansion was removed, as well as to iPS-derived MNs from patients carrying the M337V or I383T mutation in *TARDBP*.

High glutamatergic synaptic activity in ALS is believed to lead to calcium overload and eventually MN death (Cleveland and Rothstein, 2001; Pasinelli and Brown, 2006). Recent evidence shows increased Ca^{2+} permeability of AMPA receptors in *C9ORF72* iPS-derived MNs (Selvaraj et al., 2018), and influx of Ca^{2+} through AMPA-Rs and NMDA-Rs may be a signal for activating the intrinsic stress response and contributing to triggering non-AUG-dependent translation in *C9ORF72* cellular models (Westergard et al., 2019). In line with recent research, we detected increased excitability to glutamate stimulation and increased susceptibility to glutamate-induced cell death. Despite low glutamate-induced Ca^{2+} amplitudes, *C9ORF72* MNs show a higher sensitivity to extracellular glutamate by responding with Ca^{2+} waves for a prolonged period of time due to increased expression of Ca^{2+}-permeable AMPA-R subunits (*GRIA1* and *GRIA3*) and NMDA-R subunits (*GRIN2A*). Low glutamate-induced Ca^{2+} amplitudes may be explained by increased expression of *GRIA2*, which is a Ca^{2+}-impermeable AMPA subunit that has been shown to affect AMPA-induced Ca^{2+} peaks similarly in FUS iPS-derived MNs (Bursch et al., 2019), and which may be a compensatory mechanism activated by the MNs. However, there is a clear shift in the balance

Figure 5. Impairment of Mitochondrial Ca^{2+} Buffering Due to Reduced MCU and MICU2 Levels in *C9ORF72* MNs

(A and B) (A) Representative image of Rhod 2AM-loaded neurons and (B) representative Ca^{2+} traces.

(C) Ca^{2+} uptake in the mitochondria is lower in *C9ORF72* MNs compared with the C9-Ed MNs and healthy control MNs on glutamate stimulation; n = 15–62 neurons from two to three independent differentiations.

(D) Mitochondrial Ca^{2+} uptake in response to caffeine is significantly reduced in *C9ORF72* MNs (***p < 0.001); n = 8–23 neurons from two to three independent differentiations.

(E) Representative Ca^{2+} traces recorded in response to glutamate stimulation and CCCP.

(F) Amplitude of Ca^{2+} released from mitochondria is significantly lower in *C9ORF72* MNs (**p < 0.01, ***p < 0.001); n = 27–39 neurons from two independent differentiations.

(G and H) Immunoblotting of MCU (G) shows reduced levels in *C9ORF72* MNs (H) (*p < 0.05, **p < 0.01, ***p < 0.001).

(I–K) (I) RNA-seq showing *MICU2* levels are downregulated in *C9ORF72* iPS-derived MNs compared with C9-Ed and (J) immunoblotting confirming reduced expression of MICU2 in C9-02 and (K) qPCR confirming reduced *MICU2* expression (*p < 0.05, **p < 0.01, ***p < 0.001). Data are shown as mean ± SEM with one-way ANOVA and Sidak's *post hoc* tests.

See also Figure S5.

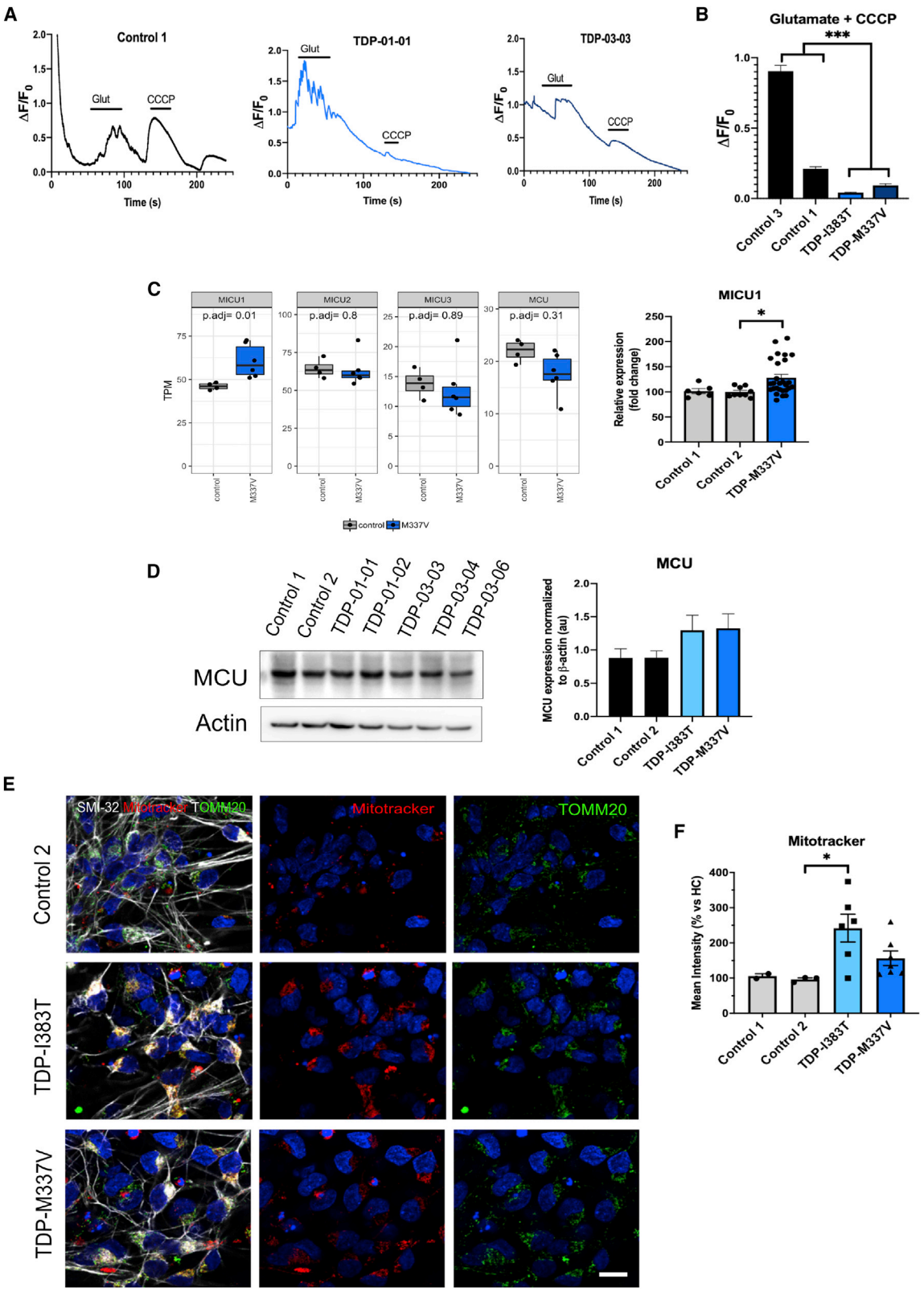

(legend on next page)

between Ca^{2+}-permeable subunits and Ca^{2+}-impermeable subunits, which also increases the recovery times in the *C9ORF72* MNs and allows Ca^{2+} entry at non-physiological levels, which is cleared at a lower rate due to low levels of the cytosolic calcium buffering protein calbindin.

TARDBP MNs carrying the M337V mutation showed upregulation of Ca^{2+}-permeable AMPA-R subunits (*GRIA4*) and NMDA-R subunits (*GRIN1* and *GRIN2B*) and a similar high frequency of Ca^{2+} waves in response to glutamate, demonstrating a similar imbalance toward increased Ca^{2+} permeability. Blocking NMDA receptors resulted in higher Ca^{2+} levels in *TARDBP* compared with *C9ORF72*, indicating that Ca^{2+} permeability of the AMPA receptors is higher in *TARDBP* than *C9ORF72*.

Although depolarization induced hyperexcitability in *C9ORF72* MNs and hypoexcitability in *TARDBP* MNs, the recovery times for both *C9ORF72* and *TARDBP* were significantly higher than healthy controls. We showed that these Ca^{2+} responses could be linked to the levels of ER Ca^{2+} stores, as we measured low ER Ca^{2+} levels in *TARDBP* MNs. Furthermore, we found that both ALS mutations were associated with reduced release of Ca^{2+} from the ER stores through IP_3R. Release through IP_3R is essential for ER-mitochondria transfer of Ca^{2+} ions that contribute to the regulation of tricarboxylic acid cycle and ATP production. Previous research has shown that there is decreased contact between the ER and mitochondria in cells carrying *FUS* and *TARDBP* mutations (Stoica et al., 2014), and, together with low ER Ca^{2+} release, could account for mitochondrial dysfunction in both mutations.

We have shown previously that the mitochondrial membrane potential is significantly reduced in the *C9ORF72* MNs (Dafinca et al., 2016), indicating a reduced capacity to take up cytosolic calcium. In line with our previous findings, we detect low mitochondrial Ca^{2+} uptake in *C9ORF72* MNs compared with both healthy and corrected MNs. Ca^{2+} entry into the mitochondria is mediated by the Ca^{2+} uniporter channel complex that contains the mitochondrial Ca^{2+} uniporter, a Ca^{2+} selective pore, and its associated regulatory proteins, MICU1 and MICU2 (Payne et al., 2017). A contributing factor to the low uptake in *C9ORF72* MNs is the reduced expression of the MCU along with reduced expression of MICU2. MICU2, together with MICU1, is located on the outer mitochondrial membrane, where it modulates and regulates Ca^{2+} affinity of the MCU channel in a complex functional interaction (Pendin et al., 2014). Although there is contradictory data in the literature with regard to their exact roles, it is generally accepted that MICU2 plays an important role in inhibiting Ca^{2+} uptake during resting state in the presence of low cytosolic Ca^{2+} levels, leading to the stabilization of mitochondrial Ca^{2+} levels (Patron et al., 2014). Consistent with our results in iPS-derived MNs, it has previously been shown that downregulation of MICU2 and MCU results in a net inhibition of Ca^{2+} uptake (Pendin et al., 2014; Plovanich et al., 2013). Therefore, the delayed buffering capacity of *C9ORF72* MNs could be explained by a reduced expression of MICU2 and MCU.

In contrast, *TARDBP* MNs show upregulation of MICU1, which provides an essential protective mechanism by limiting MCU-mediated Ca^{2+} uptake at low levels of cytosolic Ca^{2+} to limit mitochondria becoming constitutively loaded with Ca^{2+} under resting conditions (Mallilankaraman et al., 2012). Optimal stoichiometry between MICU1 and MICU2 was shown to be necessary for efficient gatekeeping of the MCU channel and mediating Ca^{2+} uptake (Payne et al., 2017). Both mutations affect the stoichiometry of MICU1 and MICU2 with the same overall result of high MICU1 compared with MICU2. Therefore, it is evident that dysregulation of the balance in these gatekeeping proteins on the mitochondrial Ca^{2+} uniporter is essential to controlling the physiological uptake of Ca^{2+} in the mitochondria and that this phenomenon is a convergent pathomechanism in ALS MNs.

In our *C9ORF72* MNs, we detected several physiological deficits in Ca^{2+} homeostasis which were reversed by the excision of the repeat expansion in CRISPR/Cas9 MNs. The cytosolic levels of free Ca^{2+} ions are significantly higher upon stimulation and we show that this is at least partly explained by reduced mitochondrial buffering of Ca^{2+} due to low expression of MCU and reduced levels of MICU2, reduced availability of the calcium binding protein calbindin, and increased expression of Ca^{2+}-permeable receptors. We show that some of these phenotypes are common to MNs derived from *TARDBP* patients, such as high expression of Ca^{2+}-permeable glutamate

Figure 6. *TARDBP* MNs Show Reductions in Mitochondrial Ca^{2+} Uptake with Increased Expression of MICU1

(A) Ca^{2+} traces after stimulation with glutamate followed by perfusion with CCCP.

(B) Mitochondrial Ca^{2+} release after CCCP is significantly lower in *TARDBP* MNs (***$p < 0.001$); n = 22–75 neurons from two to three independent differentiations.

(C) RNA-seq shows upregulation of *MICU1* and validation by qPCR (*$p < 0.05$).

(D) Immunoblotting shows no significant differences in the expression of MCU between healthy controls and TDP-43 MNs.

(E and F) MitoTracker imaging shows higher intensity in TDP-43^{I383T} (E), but no significant difference in TDP-43^{M337V} (F). Data are presented as mean ± SEM with one-way ANOVA and Sidak's *post hoc* tests.

See also Figure S6.

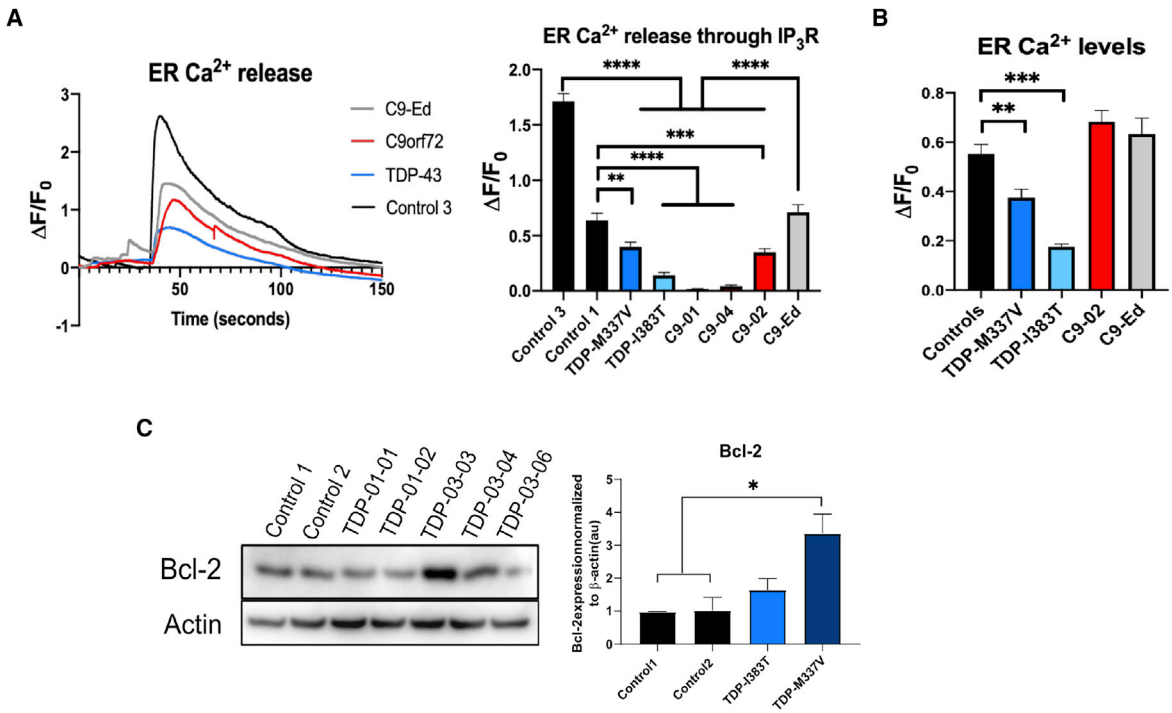

Figure 7. ER Ca^{2+} Release Is Impaired in *TARDBP* and *C9ORF72* MNs

(A) Ca^{2+} traces for TDP-43^{M337V}, TDP-43^{I383T}, C9-02, C9-Ed, and healthy MNs after stimulation with 100 μM carbachol, and quantification of the peaks shows reduced Ca^{2+} amplitudes in *TARDBP* and *C9ORF72* MNs (**p < 0.01, ***p < 0.001, ****p < 0.0001); n = 20–111 neurons from two to four independent differentiations.

(B) Measurement of ER Ca^{2+} levels shows significantly reduced levels of Ca^{2+} in *TARDBP* MNs (**p < 0.01, ***p < 0.001); n = 61–86 neurons from three independent differentiations.

(C) Immunoblotting shows a significant increase in the expression of Bcl-2 in TDP-43^{M337V} (*p < 0.05). Data are presented as mean ± SEM with one-way ANOVA and Dunnett's *post hoc* tests.

See also Figures S6 and S7.

receptors and reduced mitochondrial Ca^{2+} buffering, but differences in excitability are also evident between the two genotypes which can partly be accounted for by increased or reduced ER Ca^{2+} levels, respectively. The differences and similarities in Ca^{2+} homeostasis we identify here between *C9ORF72* and *TARDBP* mutations are an important and relevant aspect of disease. We observe these phenotypes in the absence of TDP-43 cytoplasmic mislocalization, suggesting that mislocalization may be a consequence of these dysregulations. Overall, our findings suggest that targeting dysregulation of Ca^{2+} homeostasis may be one strategy to preserve MN viability in ALS.

EXPERIMENTAL PROCEDURES

Generation of hiPSC Lines

All iPSC lines were derived from skin biopsy fibroblasts, collected under ethical approval granted by the South Wales Research Ethics Committee (WA/12/0186) in the James Martin Stem Cell Facility, University of Oxford, under standardized protocols (see Table S2). Fibroblasts and derived iPSC lines tested negative for mycoplasma (MycoAlert, Lonza, UK, www.lonza.com/). OXTDP-01 clones were derived using the Sendai virus-based reprogramming system CytoTune™ (Klf4, Oct4, Sox2, c-Myc genes in individual viruses); OXTDP-03 clones were derived using Cytotune 2.0 (polycistronic vector Klf4–Oct3/4–Sox2, cMyc, and Klf4 separate viruses) (Life Technologies, Rockville, MD, http://www.lifetech.com, used according to the manufacturer's instructions). Transduced fibroblasts were plated for generation of iPSC clones, and clones were picked, expanded, and banked as described previously (Dafinca et al., 2016).

Quality Control Assessment of hiPSC Lines

Genome integrity and identity of derived iPSC clones versus the original fibroblast pool was assessed by Illumina Human CytoSNP-12v2.1 beadchip array (300,000 markers) or Illumina HumanOmniExpress-24 (700,000 markers) and analyzed using KaryoStudio and GenomeStudio software (Illumina).

iPSC lines were assessed for expression of pluripotency markers by flow cytometry as described previously (Dafinca et al., 2016), using a FACS Calibur (Becton Dickinson, Franklin Lakes, NJ) and analyzed using FlowJo software. The following antibodies

(clone, isotype control, supplier) were used: TRA-1-60 (330614, IgM-488, BioLegend), NANOG (D73G4, IgG-647, Cell Signaling Technology).

Clearance of Sendai virus from reprogrammed cell lines was confirmed by polymerase chain reaction (PCR). RNA was extracted and reverse transcribed as described previously (Dafinca et al., 2016) with fibroblasts as negative control, and fibroblasts infected with Sendai reprogramming viruses 5 days previously as positive control. PCR was carried out according to the Cytotune manufacturers' instructions, using actin β as a positive control for each line (actin β primers, 92 bp, Eurogentec), and products were visualized by running on a 1.5% agarose gel with ethidium bromide, and 1 kB HyperLadder (Bioline https://www.bioline.com) primers: Cytotune 2.0 primers: SeV F: GGA TCA CTA GGT GAT ATC GAG C; R: ACC AGA CAA GAG TTT AAG AGA TAT GTA TC; KOS F: ATG CAC CGC TAC GAC GTG AGC GC; R: ACC TTG ACA ATC CTG ATG TGG; Klf4 F: TTC CTG CAT GCC AGA GGA GCC C; R: AAT GTA TCG AAG GTG CTC AA; c-Myc F: TAA CTG ACT AGC AGG CTT GTC G; R: TCC ACA TAC AGT CCT GGA TGA TG; Actin F AGGCATCCTCACCCTGAAG; R TCCATGCCCAGGAAGGAAG; 2-log ladder (New England Biolabs).

CRISPR/Cas9 Nuclease-Mediated Gene Editing of the G4C2 Repeat Expansion

Correction of $(G4C2)_{1000}$ repeat expansion in *C9ORF72* is described elsewhere (manuscript under review). In brief, to correct the mutation, double-nicking CRISPR/Cas9 and homology-directed repair were used on the C902-02 iPS line to remove 1,000 G_4C_2 repeats and replace them with 2 G_4C_2 repeats using 2 guide RNAs and a double-stranded DNA plasmid donor template. A Puro/TK selection cassette was also inserted in the donor template plasmid to facilitate the isolation of the corrected clones. The gRNAs, donor plasmid, and Cas9 were transfected into the C902-02 iPSCs using Neon nucleofection (Thermo Fisher Scientific). Several days after transfection, the puromycin selection was started and clones were picked and screened. After successful integration of the donor template, Cre/*loxP*-mediated excision was used to remove the Puro/TK selection cassette from the edited lines. The absence of the repeat and presence of the remaining *loxP* site in the targeted alleles was confirmed by sequencing and Southern blot analysis.

MN Differentiation and Analysis

MN differentiation was performed using a previously published protocol (Maury et al., 2015), with some modifications. In brief, the iPSCs were grown on Geltrex in mTeSR 1 supplemented with mTeSR supplement (STEMCELL Technologies) and antibiotics (Life Technologies). Induction was started when iPSCs were 90% confluent in DMEM/F12/Neurobasal medium 1:1, 1× N2 supplement, 1× B27 supplement, ascorbic acid (0.5 μM, Sigma), β-mercaptoethanol (50 μM), compound C (1 μM), and Chirr99201 (3 μM, Tocris Bioscience). On day 2, the induction medium was supplemented with all-*trans* retinoic acid (1 μM, Sigma) and Smoothened agonist (500 nM). On day 6, we removed from the medium Chirr99201 and compound C. On day 9, the neural precursors were split 1:3 using Accutase (Life Technologies), and Rock inhibitor (Tocris Bioscience) was added for 24 h. The neural precursors were maintained until day 19 in this medium and changed to the basal medium supplemented with brain-derived neurotrophic factor (10 μM, Life Technologies), glial cell line-derived neurotrophic factor (10 μM, Life Technologies), and laminin (500 ng/μL). DAPT (10 μM, Tocris Bioscience) and Rock inhibitor were added for 7 days and withdrawn for the rest of the maturation. Analysis was performed on day 30 of the differentiation protocol in all experiments.

Calcium Imaging

Calcium transients in iPS-derived MNs were measured using the fluorescent probe Fura 2-AM, Fluo 4-AM, or Rhod 2-AM according to the manufacturers protocol (Life Technologies). Neurons were incubated with 4 μM Fura 2-AM dissolved in 0.2% dimethyl sulfoxide (Sigma-Aldrich) with 0.04% pluronic acid in Hank's balanced salts solution (HBSS) supplemented with HEPES, $CaCl_2$, and $MgCl_2$ for 1 h at 37°C. Single-cell Ca^{2+} images were taken by fluorescence microscopy at room temperature. The dye was excited at 340 and 380 nm, and the emission fluorescence was collected at 510 nm. Images were taken every 30 s in a time-lapse fashion and a baseline was recorded for 30 s before stimulation. Between stimulations, cells were washed for 5 min with HBSS supplemented with HEPES. Neurons were incubated with 20 μM Fluo 4-AM in 0.2% dimethyl sulfoxide and 0.04% pluronic acid for 30 min at room temperature in HBSS supplemented with HEPES, $CaCl_2$, and $MgCl_2$. The dye was excited at 488 nm and images were taken every 30 s in a time-lapse fashion with a baseline recorded for 30 s before stimulation.

The stimuli used for calcium release were 50 mM KCl (Sigma), 1 mM L-glutamic acid (Sigma), 4 μM CCCP (Tocris Bioscience), 20 mM caffeine (Tocris Bioscience), 100 μM CNQX (Tocris Bioscience), and 10 μM memantine (Tocris Bioscience). Analysis of fluorescence intensity was performed using ImageJ and FIJI. Fluorescence measurements are expressed as a ratio ($\Delta F/F_o$) of the mean change in fluorescence (ΔF) at a pixel relative to the resting fluorescence at that pixel before stimulation (F_o). For each recording, the soma of neuronal looking cells was selected as a region of interest and up to 25 neurons per recording were selected. The fluorescence intensity was plotted for each neuron against frame number and the y values representing F_0 (start of response) and F_1 (peak response) were manually copied. The recovery time was analyzed from the x axis values representing the frame number at peak fluorescence and the frame number when fluorescence intensity returned to F_0.

Mitochondrial and ER Ca^{2+} Imaging

Neurons were loaded with 4 μM Rhod 2-AM for 45 min at 37°C. The neurons were imaged as described above, using excitation at 567 nm. Image analysis was performed using FIJI and GraphPad Prism, as described above.

For ER Ca^{2+} imaging, MNs were loaded with 20 μM Fluo 4-AM in 0.2% DMSO and 0.04% pluronic acid for 30 min at room temperature in HBSS supplemented with HEPES, $CaCl_2$, and $MgCl_2$. For ER Ca^{2+} release, neurons were recorded for 30 s under continuous perfusion of HBSS followed by 30 s of 50 μM carbachol in HBSS depleted of $CaCl_2$ and $MgCl_2$. The neurons were then washed in

HBSS with $CaCl_2$ and $MgCl_2$. For measurement of ER Ca^{2+} levels, the neurons were loaded on to the microscope and washed in HBSS depleted of $CaCl_2$ and $MgCl_2$, and 10 μM thapsigargin were added directly to the coverslip.

Image analysis was performed using FIJI and GraphPad Prism, as described above.

Immunofluorescence

Mature MNs were fixed with 4% paraformaldehyde-PBS for 15 min and incubated with 10% donkey serum for blocking for 1 h at room temperature. The cells were incubated overnight at 4°C with rabbit anti-TOMM20 (Abcam 78547, 1:500), mouse or rabbit anti-β-III Tubulin (Tuj1) (Covance MMS-435P, PRB-435P; 1:1,000), mouse anti-SMI-32 (Covance 801701, 1:1,000). After washing with 0.1% Triton X-/PBS three times for 10 min, the samples were incubated with Alexa Fluor 488-, Alexa Fluor 568-, and Alexa Fluor 647-conjugated donkey anti-rabbit, anti-mouse, or anti-goat secondary antibodies (Life Technologies A32766, A10042, and A32849) for 1 h at room temperature. Nuclei were stained with DAPI. Fluorescence was visualized using a confocal microscope Zeiss LSM.

Protein Extraction and Western Blotting

Cells were lysed in RIPA buffer (Sigma), sonicated, and incubated on ice. After centrifugation at 3,000 × *g* for 10 min, the supernatant was retained and protein concentration was quantified using the bicinchoninic acid assay (Sigma). Protein was loaded and resolved on SDS-PAGE (4%–12% Tris-glycine gel) using a Mini-PROTEAN electrophoresis system (Life Technologies) under constant current and transferred to a methanol-activated polyvinylidene difluoride membrane (Immobilon-P) using the Novex Blot system under constant voltage (100 mA for 70 min). Blots were transferred to blocking buffer (Tris-buffered saline [TBS], 0.1% Tween 20, 5% skimmed milk) for 1 h at room temperature and incubated in TBS + 0.1% Tween 20 + 1% milk with primary antibodies. Primary antibodies used were mouse anti-MCU (Abcam ab219827, 1:500), mouse anti-calbindin (Abcam ab108404; 1:1,000), rabbit anti-calreticulin (Abcam ab2907; 1:500), mouse anti-calnexin (Abcam ab112995, 1:500), rabbit anti-calpain-1 (Abcam ab39170, 1:500), rabbit anti-inositol-1,4,5-triphosphate receptor (Abcam ab5804, 1:300), and mouse anti-β-actin (Sigma A5441, 1:5,000). Horseradish peroxidase-conjugated anti-mouse IgG or anti-rabbit IgG (Life Technologies, G1040 and G1234) were used as secondary antibodies and the signal was visualized using an ECL or ECL Plus detection system (Millipore) on a Bio-Rad ChemiDoc. The integrated optical density of each band was measured in ImageJ and expression was normalized to β-actin levels in the same blot for comparative expression assessment.

RNA Sequencing

RNA sequencing and analysis was performed as described elsewhere (manuscript under review). In brief, RNA was extracted from samples from whole MN cultures at day 28. Library preparation was performed using the paired-end Illumina TruSeq sample preparation kit and samples were run on the Illumina HiSeq 4000 sequencer for 75 cycles. Samples underwent extensive quality control, and two samples with significant biases were removed from the analysis. A total of four samples derived from cell line C9-02-02, three samples from cell line C9-Ed-02-01, and three samples from cell line C9-Ed-02-02 were used in this analysis. Three samples derived from two healthy control lines (180 and 840) were also used. A counts table and normalized abundances in the form of transcripts per million were obtained using *Salmon*. Differential expression analysis was performed using *DESeq2* taking into account operator bias in the linear model. Benjamini-Hochberg corrected p values were reported for the differential expression analysis.

The data discussed in this publication have been deposited in NCBI's Gene Expression Omnibus and are accessible under GEO series accession number NCBI: GSE147544 (https://www.ncbi.nlm.nih.gov/geo/query/acc.cgi?acc=GSE147544) and NCBI: GSE139144 (https://www.ncbi.nlm.nih.gov/geo/query/acc.cgi?acc=GSE139144).

qPCR

RNA sequencing results were validated on an extended sample cohort for the *C9ORF72* MNs (two genome-edited samples, three control samples, six C9-02-02 and C9-02-03 samples, one C9-04-01, and one C9-01-06, coming from three independent differentiations). For validation of RNA sequencing of TDP-43^{M337V} MNs, we used five healthy controls and three M337V clones (TDP-03-03, TDP-03-04, and TDP-03-06) from three independent differentiations. RNA extraction was performed using the RNeasy Mini Kit (QIAGEN), following the manufacturer's instructions, and cDNA was prepared using the High-Capacity cDNA Reverse Transcription Kit (Thermo Fisher Scientific). qPCR was performed using the Fast SYBR Green Master Mix (Thermo Fisher Scientific) using 0.2 μL of cDNA and 250 μM primers (Table S1). Samples (10 μL) were run in triplicate on the LightCycler 480 (Roche). Three reference genes were used for all reactions (TOP1, GAPDH, and ATP5B) and the geometric mean of all three genes was used as the reference for gene expression estimation. Relative abundance estimation was carried out using the $2^{-\Delta\Delta Ct}$ method.

Statistical Analyses

At least two independent differentiations were performed for every experiment shown and data pooled from at least three independent cultures. For TDP-43 MNs, results from three clones of one TDP-M337V patient are grouped together (TDP-03-03, TDP-03-04, and TDP-03-06) and two clones (01-01 and 01-02) are grouped for TDP-I383T. For groups of three or more, ANOVAs were performed with relevant corrections for multiple comparisons. All statistical analyses were done using GraphPad Prism 8.

SUPPLEMENTAL INFORMATION

Supplemental Information can be found online at https://doi.org/10.1016/j.stemcr.2020.03.023.

AUTHOR CONTRIBUTIONS

R.D. conceived the idea, designed, performed, and interpreted most of the experiments. P.B. performed some of the data acquisition and analysis (immunoblotting). L.F. performed qPCR validations, analysis, and immunoblotting. A.C. performed some of the data acquisition, interpretation, and iPS differentiations to

motor neurons. J.S. performed and analyzed RNA sequencing results. N.A.A. generated the genome-edited iPS line and reprogrammed fibroblasts to iPS. C.S. aided with qPCR validations. J.V. and S.A.C. reprogrammed fibroblasts to iPSCs. R.D. and K.T. interpreted the results and wrote the manuscript.

ACKNOWLEDGMENTS

The work was funded by the Motor Neurone Disease Association (grant numbers 832/791, 889-792, and 886-792). J.S. was funded by an MRC/MND Association Lady Edith Wolfson Fellowship. N.A.A. was funded by the University of Jordan. The James Martin Stem Cell Facility, University of Oxford, is financially supported by the Wellcome Trust (WTISSF121302) and the Oxford Martin School (LC0910-004). J.V. and S.A.C. are supported by the Monument Trust Discovery Award from Parkinson's UK, a charity registered in England and Wales (2581970) and in Scotland (SC037554).

Received: August 4, 2019
Revised: March 25, 2020
Accepted: March 26, 2020
Published: April 23, 2020

REFERENCES

Bursch, F., Kalmbach, N., Naujock, M., Staege, S., Eggenschwiler, R., Abo-Rady, M., Japtok, J., Guo, W., Hensel, N., Reinhardt, P., et al. (2019). Altered calcium dynamics and glutamate receptor properties in iPSC derived motor neurons from ALS patients with C9orf72, FUS, SOD1 or TDP43 mutations. Hum. Mol. Genet *28*, 2835–2850.

Cleveland, D.W., and Rothstein, J.D. (2001). From Charcot to Lou Gehrig: deciphering selective motor neuron death in ALS. Nat. Rev. Neurosci. *2*, 806–819.

Couratier, P., Hugon, J., Sindou, P., Vallat, J.M., and Dumas, M. (1993). Cell culture evidence for neuronal degeneration in amyotrophic lateral sclerosis being linked to glutamate AMPA/kainate receptors. Lancet *341*, 265–268.

Dafinca, R., Scaber, J., Ababneh, N., Lalic, T., Weir, G., Christian, H., Vowles, J., Douglas, A.G., Fletcher-Jones, A., Browne, C., et al. (2016). C9orf72 hexanucleotide expansions are associated with altered endoplasmic reticulum calcium homeostasis and stress granule formation in induced pluripotent stem cell-derived neurons from patients with amyotrophic lateral sclerosis and frontotemporal dementia. Stem Cells *34*, 2063–2078.

Dedeene, L., Van Schoor, E., Race, V., Moisse, M., Vandenberghe, R., Poesen, K., Van Damme, P., and Thal, D.R. (2019). An ALS case with 38 (G4C2)-repeats in the C9orf72 gene shows TDP-43 and sparse dipeptide repeat protein pathology. Acta Neuropathol. *137*, 855–858.

DeJesus-Hernandez, M., Mackenzie, I.R., Boeve, B.F., Boxer, A.L., Baker, M., Rutherford, N.J., Nicholson, A.M., Finch, N.A., Flynn, H., Adamson, J., et al. (2011). Expanded GGGGCC hexanucleotide repeat in noncoding region of C9ORF72 causes chromosome 9p-linked FTD and ALS. Neuron *72*, 245–256.

Devlin, A.C., Burr, K., Borooah, S., Foster, J.D., Cleary, E.M., Geti, I., Vallier, L., Shaw, C.E., Chandran, S., and Miles, G.B. (2015). Human iPSC-derived motoneurons harbouring TARDBP or C9ORF72 ALS mutations are dysfunctional despite maintaining viability. Nat. Commun. *6*, 5999.

Donnelly, C.J., Zhang, P.W., Pham, J.T., Haeusler, A.R., Mistry, N.A., Vidensky, S., Daley, E.L., Poth, E.M., Hoover, B., Fines, D.M., et al. (2013). RNA toxicity from the ALS/FTD C9ORF72 expansion is mitigated by antisense intervention. Neuron *80*, 415–428.

Filadi, R., Theurey, P., and Pizzo, P. (2017). The endoplasmic reticulum-mitochondria coupling in health and disease: molecules, functions and significance. Cell Calcium *62*, 1–15.

Herrington, J., Park, Y.B., Babcock, D.F., and Hille, B. (1996). Dominant role of mitochondria in clearance of large Ca^{2+} loads from rat adrenal chromaffin cells. Neuron *16*, 219–228.

Majounie, E., Renton, A.E., Mok, K., Dopper, E.G., Waite, A., Rollinson, S., Chio, A., Restagno, G., Nicolaou, N., Simon-Sanchez, J., et al. (2012). Frequency of the C9orf72 hexanucleotide repeat expansion in patients with amyotrophic lateral sclerosis and frontotemporal dementia: a cross-sectional study. Lancet Neurol. *11*, 323–330.

Mallilankaraman, K., Doonan, P., Cardenas, C., Chandramoorthy, H.C., Muller, M., Miller, R., Hoffman, N.E., Gandhirajan, R.K., Molgo, J., Birnbaum, M.J., et al. (2012). MICU1 is an essential gatekeeper for MCU-mediated mitochondrial Ca(2+) uptake that regulates cell survival. Cell *151*, 630–644.

Maury, Y., Come, J., Piskorowski, R.A., Salah-Mohellibi, N., Chevaleyre, V., Peschanski, M., Martinat, C., and Nedelec, S. (2015). Combinatorial analysis of developmental cues efficiently converts human pluripotent stem cells into multiple neuronal subtypes. Nat. Biotechnol. *33*, 89–96.

Mutihac, R., Alegre-Abarrategui, J., Gordon, D., Farrimond, L., Yamasaki-Mann, M., Talbot, K., and Wade-Martins, R. (2015). TARDBP pathogenic mutations increase cytoplasmic translocation of TDP-43 and cause reduction of endoplasmic reticulum Ca(2)(+) signaling in motor neurons. Neurobiol. Dis. *75*, 64–77.

Pasinelli, P., and Brown, R.H. (2006). Molecular biology of amyotrophic lateral sclerosis: insights from genetics. Nat. Rev. Neurosci. *7*, 710–723.

Patron, M., Checchetto, V., Raffaello, A., Teardo, E., Reane, D.V., Mantoan, M., Granatiero, V., Szabo, I., De Stefani, D., and Rizzuto, R. (2014). MICU1 and MICU2 finely tune the mitochondrial Ca^{2+} uniporter by exerting opposite effects on MCU activity. Mol. Cell *53*, 726–737.

Payne, R., Hoff, H., Roskowski, A., and Foskett, J.K. (2017). MICU2 restricts spatial crosstalk between InsP3R and MCU channels by regulating threshold and gain of MICU1-mediated inhibition and activation of MCU. Cell Rep. *21*, 3141–3154.

Pendin, D., Greotti, E., and Pozzan, T. (2014). The elusive importance of being a mitochondrial Ca(2+) uniporter. Cell Calcium *55*, 139–145.

Peng, T.I., Jou, M.J., Sheu, S.S., and Greenamyre, J.T. (1998). Visualization of NMDA receptor-induced mitochondrial calcium accumulation in striatal neurons. Exp. Neurol. *149*, 1–12.

Plovanich, M., Bogorad, R.L., Sancak, Y., Kamer, K.J., Strittmatter, L., Li, A.A., Girgis, H.S., Kuchimanchi, S., De Groot, J., Speciner, L., et al. (2013). MICU2, a paralog of MICU1, resides within the mitochondrial uniporter complex to regulate calcium handling. PLoS One *8*, e55785.

Renton, A.E., Majounie, E., Waite, A., Simon-Sanchez, J., Rollinson, S., Gibbs, J.R., Schymick, J.C., Laaksovirta, H., van Swieten, J.C., Myllykangas, L., et al. (2011). A hexanucleotide repeat expansion in C9ORF72 is the cause of chromosome 9p21-linked ALS-FTD. Neuron *72*, 257–268.

Rothstein, J.D., Martin, L.J., and Kuncl, R.W. (1992). Decreased glutamate transport by the brain and spinal cord in amyotrophic lateral sclerosis. N. Engl. J. Med. *326*, 1464–1468.

Rothstein, J.D., Tsai, G., Kuncl, R.W., Clawson, L., Cornblath, D.R., Drachman, D.B., Pestronk, A., Stauch, B.L., and Coyle, J.T. (1990). Abnormal excitatory amino acid metabolism in amyotrophic lateral sclerosis. Ann. Neurol. *28*, 18–25.

Sareen, D., O'Rourke, J.G., Meera, P., Muhammad, A.K., Grant, S., Simpkinson, M., Bell, S., Carmona, S., Ornelas, L., Sahabian, A., et al. (2013). Targeting RNA foci in iPSC-derived motor neurons from ALS patients with a C9ORF72 repeat expansion. Sci. Transl. Med. *5*, 208ra149.

Selvaraj, B.T., Livesey, M.R., Zhao, C., Gregory, J.M., James, O.T., Cleary, E.M., Chouhan, A.K., Gane, A.B., Perkins, E.M., Dando, O., et al. (2018). C9ORF72 repeat expansion causes vulnerability of motor neurons to Ca^{2+}-permeable AMPA receptor-mediated excitotoxicity. Nat. Commun. *9*, 347.

Stoica, R., De Vos, K.J., Paillusson, S., Mueller, S., Sancho, R.M., Lau, K.F., Vizcay-Barrena, G., Lin, W.L., Xu, Y.F., Lewis, J., et al. (2014). ER-mitochondria associations are regulated by the VAPB-PTPIP51 interaction and are disrupted by ALS/FTD-associated TDP-43. Nat. Commun. *5*, 3996.

van der Zee, J., Gijselinck, I., Dillen, L., Van Langenhove, T., Theuns, J., Engelborghs, S., Philtjens, S., Vandenbulcke, M., Sleegers, K., Sieben, A., et al. (2013). A pan-European study of the C9orf72 repeat associated with FTLD: geographic prevalence, genomic instability, and intermediate repeats. Hum. Mutat. *34*, 363–373.

Werth, J.L., and Thayer, S.A. (1994). Mitochondria buffer physiological calcium loads in cultured rat dorsal root ganglion neurons. J. Neurosci. *14*, 348–356.

Westergard, T., McAvoy, K., Russell, K., Wen, X., Pang, Y., Morris, B., Pasinelli, P., Trotti, D., and Haeusler, A. (2019). Repeat-associated non-AUG translation in C9orf72-ALS/FTD is driven by neuronal excitation and stress. EMBO Mol. Med. *11*. https://doi.org/10.15252/emmm.201809423.